



Real-time dual-sensitive shearography for simultaneous in-plane and out-of-plane strain measurements

JIE DONG,^{1,*} SHENGJIA WANG,¹ MIN LU,¹ MARTIN JAKOBI,¹
ZHANWEI LIU,^{2,4} XINGCHEN DONG,¹ FRANZISKA PÖLLER,¹ LAURA
MARIA BILGERI,¹ FÉLIX SALAZAR BLOISE,³ ALI K. YETISEN,¹ AND
ALEXANDER WALTER KOCH¹

¹*Institute for Measurement Systems and Sensor Technology, Technical University of Munich, Arcisstraße 21, Munich 80333, Germany*

²*School of Aerospace Engineering, Beijing Institute of Technology, Beijing 100081, China*

³*ETSI Minas y Energía, Universidad Politécnica de Madrid, Ríos Rosas 21, Madrid 28003, Spain*

⁴*liuzw@bit.edu.cn*

**jie.dong@tum.de*

Abstract: A real-time, dual-sensitive shearography system using a single-wavelength laser was developed for simultaneous and dynamic in-plane and out-of-plane strain measurements. The shearography system is capable of measuring crack-tip deformation fields quantitatively. A spatial multiplexing technique based on Fourier transform is employed for simultaneous and dynamic multi-component phase retrieval. Two slit spatial filters and a common-path shearing interferometer are used to obtain an improved phase quality for crack-tip deformation measurements. Mode-I fracture experiments under three-point bending were conducted to validate the feasibility and the capability of this method.

© 2019 Optical Society of America under the terms of the [OSA Open Access Publishing Agreement](#)

1. Introduction

Holography and shearography are whole-field, non-invasive optical interferometric methods that allow measuring shape [1–5], displacement [6–8], strain [9, 10], and curvature [11] of a surface. They have the capability of simultaneous multi-component analyses [12–14]. Classified by sensitivity, speckle interferometry for multi-component measurements can be divided into single-sensitive and multi-sensitive techniques. Typically, single-sensitive techniques are out-of-plane sensitive, and they can be used to measure different order derivatives of the out-of-plane displacement such as simultaneous measurements of displacement and slope [12, 15], or slope and curvature [16, 17]. Without out-of-plane sensitivity limitations, multi-sensitive techniques generally have both in-plane and out-of-plane sensitivities [14, 18–22], or 3D sensitivity [14, 23]. Conventional in-plane-sensitive speckle interferometry generally requires two symmetric sensitivity vectors to obtain a pure in-plane sensitivity, so that the symmetric dual-beam system is commonly used for in-plane displacement or in-plane strain measurements [6, 24, 25]. This symmetric system can be both, in-plane- and out-of-plane-sensitive [19, 26]. However, simultaneous quantitative phase retrieval for two symmetric sensitivity vectors is still challenging, especially for in-plane strain measurements. To measure dynamic in-plane displacement, several attempts have been made based on spatial-carrier phase shifting [25], different wavelengths [27], polarization [24], different coherence lengths [28], and spatial multiplexing [20]. For in-plane strain measurements, two-step symmetric measurements and temporal phase shifting have been realized [18, 21, 22, 26, 29].

In this paper, a real-time dual-sensitive shearography system with two symmetric observation beams and one illumination beam is developed for simultaneous dynamic in-plane and out-

of-plane strain measurements. A spatial multiplexing method based on Fourier transform is introduced for multiple phase retrieval. The synchronous interferograms with the same spatial-carrier frequency but different sensitivity vectors are separated spatially. Two slit spatial filters and a common-path shearing interferometer are employed to increase phase quality. To verify the feasibility and the capability of the developed method, simultaneous in-plane and out-of-plane strain component measurements were carried out for Mode-I fracture under three-point bending.

2. Theory

2.1. Symmetric dual-sensitive shearography

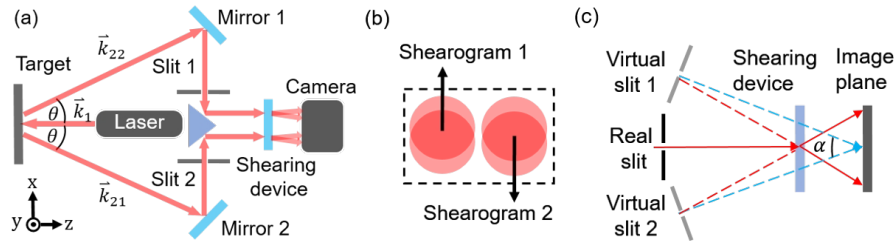


Fig. 1. Symmetric dual-sensitive shearography. (a) Schematic of the optical shearography setup. (b) Shearograms obtained using the shearography system. (c) Spatial-carrier frequency generated by the common-path shearing device.

The schematic of the real-time dual-sensitive shearography system is depicted in Fig. 1. The sample to be measured is illuminated by a collimated laser beam that is perpendicular to the sample surface. The sample is observed from two symmetric directions at equal angles θ to the z -axis. Assuming the observation direction lies in the plane $y=0$, the wave vectors of the illuminating beam \vec{k}_1 and two observation beams \vec{k}_{21} , \vec{k}_{22} can be expressed as:

$$\vec{k}_1 = \frac{2\pi}{\lambda}(-\vec{w}_0), \quad (1)$$

$$\vec{k}_{21} = \frac{2\pi}{\lambda}(-\sin\theta \cdot \vec{u}_0 + \cos\theta \cdot \vec{w}_0), \quad (2)$$

$$\vec{k}_{22} = \frac{2\pi}{\lambda}(\sin\theta \cdot \vec{u}_0 + \cos\theta \cdot \vec{w}_0), \quad (3)$$

where λ is the wavelength of the laser beam, and \vec{u}_0 , \vec{v}_0 , and \vec{w}_0 are the unit vectors along the positive x -, y -, and z - axes, respectively. Before reaching the camera, the two object beams are reflected by mirrors symmetrically and splitted into two separate and parallel paths, as shown in Fig. 1(a). Subsequently the beams pass through a common-path shearing device which introduces a variable shear in the x - and y - directions. The shearograms are shown in Fig. 1(b). During the deformation, the phase changes relating to the left observation direction \vec{k}_{21} and right observation direction \vec{k}_{22} are different. The phase change of the left vertical shearogram $\Delta\varphi_l$ is [14, 26]:

$$\begin{aligned} \Delta\varphi_l &= \vec{k}_l(\vec{u}, \vec{v}, \vec{w}) \cdot \Delta\vec{l}(x, y) \\ &= [(\vec{k}_1 - \vec{k}_{21})|_{(x,y)} - (\vec{k}_1 - \vec{k}_{21})|_{(x,y+\Delta y)}] \cdot (\Delta l_x \cdot \vec{u}_0 + \Delta l_y \cdot \vec{v}_0 + \Delta l_z \cdot \vec{w}_0) \\ &= -\frac{2\pi}{\lambda} \left[\sin\theta \cdot \frac{\partial \Delta l_x}{\partial y} - (1 + \cos\theta) \frac{\partial \Delta l_z}{\partial y} \right] \Delta y, \end{aligned} \quad (4)$$

where \vec{k}_l is the sensitivity vector relating to the left observation beam \vec{k}_{21} and the illuminating beam \vec{k}_1 . Δ_x , Δ_y , and Δ_z are the x -, y -, and z - components of the object deformation, respectively. Δy is the shearing amount.

Similarly, the phase change of the right vertical shearogram $\Delta\varphi_r$ is:

$$\begin{aligned}\Delta\varphi_r &= \vec{k}_r(\vec{u}, \vec{v}, \vec{w}) \cdot \Delta\vec{l}(x, y) \\ &= [(\vec{k}_1 - \vec{k}_{22})|_{(x,y)} - (\vec{k}_1 - \vec{k}_{22})|_{(x,y+\Delta y)}] \cdot (\Delta l_x \cdot \vec{u}_0 + \Delta l_y \cdot \vec{y}_0 + \Delta l_z \cdot \vec{w}_0) \\ &= \frac{2\pi}{\lambda} \left[\sin\theta \cdot \frac{\partial\Delta l_x}{\Delta y} + (1 + \cos\theta) \frac{\partial\Delta l_z}{\Delta y} \right] \Delta y,\end{aligned}\quad (5)$$

where \vec{k}_r is the sensitivity vector due to the right observation direction \vec{k}_{22} and the illuminating beam \vec{k}_1 .

$\Delta\varphi_l$ and $\Delta\varphi_r$ are both in-plane and out-of-plane sensitive. The pure out-of-plane strain component $\partial\Delta l_z/\partial y$ is determined by adding $\Delta\varphi_l$ and $\Delta\varphi_r$:

$$\Delta\varphi_l + \Delta\varphi_r = \frac{4\pi}{\lambda} \left[(1 + \cos\theta) \frac{\partial\Delta l_z}{\Delta y} \right] \Delta y.\quad (6)$$

Furthermore, the pure x -direction in-plane strain component $\partial\Delta l_x/\Delta y$ is determined by subtracting $\Delta\varphi_l$ and $\Delta\varphi_r$:

$$\Delta\varphi_l - \Delta\varphi_r = -\frac{4\pi}{\lambda} \left[(\sin\theta) \frac{\partial\Delta l_x}{\Delta y} \right] \Delta y.\quad (7)$$

In addition, by adjusting the observation direction to the plane $x=0$, the y -direction in-plane strain can be also obtained. Besides, by adjusting the shear direction, the required derivative of displacement can be measured.

2.2. Spatial multiplexing based on Fourier transform

During the measurements, the object is observed in two symmetric directions simultaneously, as shown in Fig. 1(a). The real-time multiple phase information can be extracted by using a spatial multiplexing method based on Fourier transform [20]. It was assumed that the two splitted object beams relating to the left observation incident on the detector at equal angle α to the normal vector of the imaging sensor plane, as shown in Fig. 1(c). Their individual wavefronts $u_{11}(x, y)$ and $u_{12}(x, y)$ can be expressed as:

$$u_{11}(x, y) = |u_{11}(x, y)| e^{[i\varphi(x,y) + i2\pi y f_y]},\quad (8)$$

$$u_{12}(x, y + \Delta y) = |u_{12}(x, y + \Delta y)| e^{[i\varphi(x,y+\Delta y) - i2\pi y f_y]},\quad (9)$$

where $|u_{11}(x, y)|$ and $|u_{12}(x, y + \Delta y)|$ are the amplitudes modulus of these two object beams. f_y equals to $\sin(\alpha/2)/\lambda$, which is the spatial-carrier frequency introduced by the common-path shearing device. The intensity of the left shearogram $I_l(x, y)$ is given by [30]:

$$\begin{aligned}I_l(x, y) &= [u_{11}(x, y) + u_{12}(x, y + \Delta y)] \cdot [u_{11}(x, y) + u_{12}(x, y + \Delta y)]^* \\ &= u_{11}(x, y) \cdot u_{11}^*(x, y) + u_{12}(x, y) \cdot u_{12}^*(x, y) \\ &\quad + u_{11}(x, y) \cdot u_{12}^*(x, y) + u_{12}(x, y) \cdot u_{11}^*(x, y),\end{aligned}\quad (10)$$

where $u_{11}^*(x, y)$ denotes the complex conjugate of $u_{11}(x, y)$. By using fast Fourier transform, the intensity image is transformed from the space domain into the frequency domain:

$$FT(I_l) = DC + U_{11}(f_x, f_y) \otimes U_{12}^*(f_x, f_y + f_0) + U_{12}(f_x, f_y + f_0) \otimes U_{11}^*(f_x, f_y),\quad (11)$$

where \otimes denotes the convolution operation. DC equals $U_{11}(f_x, f_y) \otimes U_{11}^*(f_x, f_y) + U_{12}(f_x, f_y + f_0) \otimes U_{12}^*(f_x, f_y + f_0)$, and it represents the direct-current component of the image. $U_{11}^*(f_x, f_y) \otimes U_{12}(f_x, f_y + f_0)$ and $U_{12}^*(f_x, f_y + f_0) \otimes U_{11}(f_x, f_y)$ contain the phase information of the shearograms. After the direct-current component of spectrum $FT(I_l)$ is eliminated, $U_{11}^*(f_x, f_y) \otimes U_{12}(f_x, f_y + f_0)$ or $U_{12}^*(f_x, f_y + f_0) \otimes U_{11}(f_x, f_y)$ will be presented by an inverse Fourier transform to get the phase distribution of the shearogram. The phase change due to the object deformation can be calculated by:

$$\Delta \varphi_l(x, y + \Delta y) = \Delta \tan^{-1} \frac{Im[u_{11} \cdot u_{12}^*]}{Re[u_{11} \cdot u_{12}^*]}. \quad (12)$$

In this system, the left shearogram and the right shearogram, which comprise different sensitivity vectors but the same carrier frequency, are recorded separately by the same camera. The phase change of the right shearogram $\Delta \varphi_r$ is given by:

$$\Delta \varphi_r(x, y + \Delta y) = \Delta \tan^{-1} \frac{Im[u_{21} \cdot u_{22}^*]}{Re[u_{21} \cdot u_{22}^*]}. \quad (13)$$

3. Experimental results and discussions

3.1. Optical setup of the dual-sensitive shearography

Figure 2 illustrates the experimental setup for the real-time dual-sensitive shearography system. A He-Ne laser (HNLS008L-EC, Thorlabs) with a wavelength of 632.8 nm and a power of 0.8 mW was used as the light source. The laser beam was expanded and collimated by two lenses with focal lengths of -6 mm and 100 mm, respectively. The beam splitter 1 was used to ensure that the illuminating beam was perpendicular to the object surface. The mirror 1/2 and the beam splitter 2/3 were used to adjust two observation beams parallel to each other and perpendicular to the camera. A Wollaston prism was employed as a shearing device, and the two polarizers enabled forming the splitted object beams with the same light intensity to obtain higher contrast fringes in the shearogram. The shearing amount could be adjusted by changing the distance between the image plane and the shearing device. A CMOS camera (DCC1545M, Thorlabs) was used as the detector, and the two slits were used as spatial filters. The spectra corresponding to the left, the right, and the resulting shearogram are shown in Figs. 2(a)-2(c), respectively. These spectra were adjusted to be identical. The system was calibrated before sample testing. During the calibration, all the features on the sample were observed clearly, including the location of crack tips. The position difference between the left and the right shearogram was calculated to ensure that a pixel level image matching was performed during the phase maps adding and subtracting.

3.2. Three-point bending fracture test

A mode-I fracture test under three-point bending was chosen for the experimental demonstration. The deformation generator is shown in Fig. 3. To satisfy the small-scale yielding, PMMA substrate with a higher yield strength was used as the model material. A specimen ($105 \times 40 \times 10 \text{ mm}^3$) with a notch ($1 \times 15 \times 10 \text{ mm}^3$) has been coated with white spray paint to increase its reflectivity. Then, it was loaded by a symmetric three-point bending with a vertical force in the center. A micrometer head was used as the loading device.

The in-plane and out-of-plane strain fields on the crack-tip area were measured simultaneously. By using the spatial multiplexing method based on Fourier transform, the wrapped 2π -modulo phase maps, which correspond to the shearograms in Fig. 1(b), were obtained, as shown in Fig. 4. Both of these two phase maps were combinations of in-plane and out-of-plane strains in accordance with Eqs. (12) and (13). These two coupled phase maps were acquired through vertical shearing that was parallel to the notch direction. The points 1 and 2 in Fig. 4(a) are the

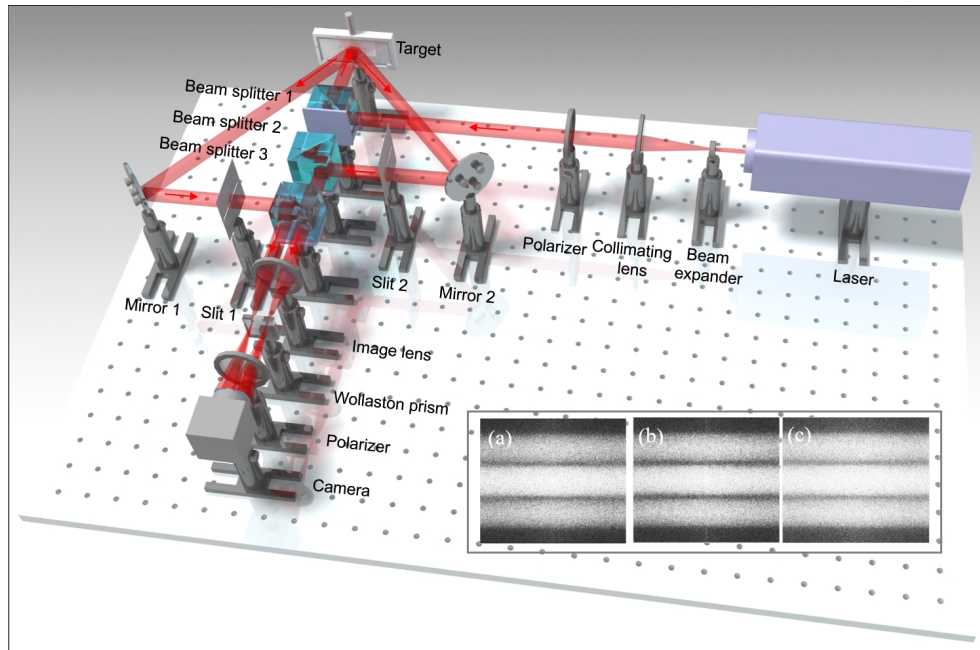


Fig. 2. Experimental setup. The spectrum maps acquired from the left (a) and right (b) channels of the interferometer and the resulting spectrum (c).

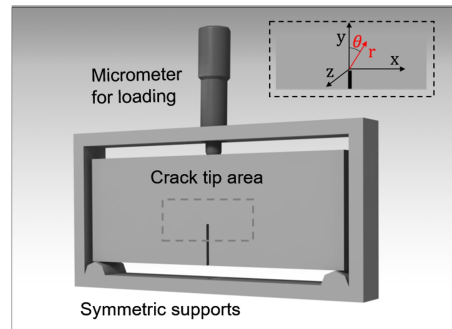


Fig. 3. The three-point bending fracture test setup and the PMMA specimen ($105 \times 40 \times 10 \text{ mm}^3$).

sheared crack-tips of the two object beams u_{11} and u_{12} .

The corresponding in-plane and out-of-plane strain fields of the surface were obtained by adding and subtracting the coupled phase maps in Figs. 4(a) and 4(b), in accordance with Eqs. (6) and (7). Pixel level image matching between the coupled phase maps was ensured during the adding and subtracting, because the position difference between the left and the right shearogram was calibrated. Figure 5(a) shows a whole field phase map of the out-of-plane strain component $\partial \Delta l_z / \partial y$ obtained through the addition of the complementary phase maps shown in Fig. 4. Here, the physical shearing amount Δy approximately equals to 4 mm , so each 2π -phase fringe corresponds to a strain difference of 46×10^{-6} according to Eq. (6). Figure 5(c) shows the in-plane strain component $\partial \Delta l_x / \Delta y$ obtained through subtraction of the two phase maps, and each 2π -phase fringe corresponds to a strain difference of 112×10^{-6} .

To verify the reliability of the measurement results, the 3D simulated strains on the crack tip of

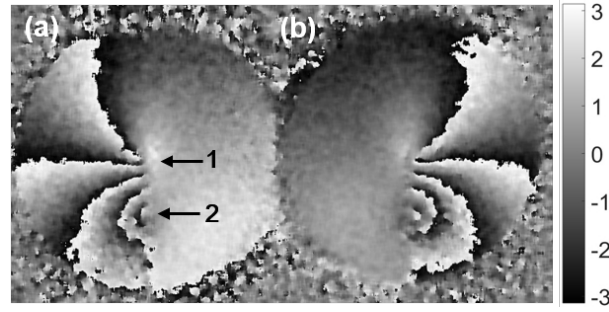


Fig. 4. Out-of-plane and in-plane coupled phase maps relating to the left (a) and right (b) sensitivity vectors, respectively.

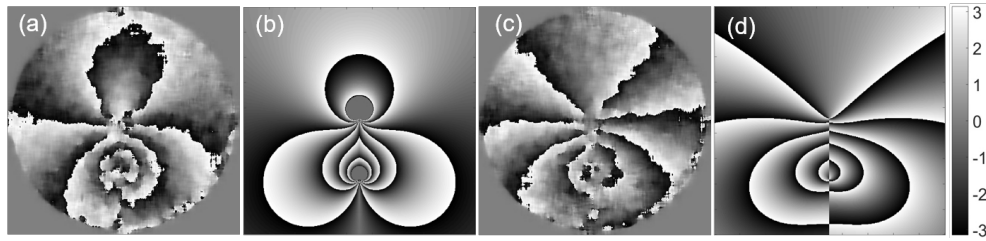


Fig. 5. Measured phase maps relating to the out-of-plane crack-tip strain component (a) $\partial \Delta l_z / \Delta y$, and the in-plane crack-tip strain component (c) $\partial \Delta l_x / \Delta y$. Analytical solutions (b) $\partial \Delta l_z / \Delta y$ and (d) $\partial \Delta l_x / \Delta y$ by linear elastic fracture mechanics.

mode-I fracture under three-point bending were obtained, as shown in Figs. 5(b) and 5(d), by the theory of linear elastic fracture mechanics. The coordinate system for the simulation is shown in Fig. 3. For the pure mode-I fracture, the plane stress predictions for the displacement fields U , V , and W are given by [21, 22, 31]:

$$U = \frac{(1 + \nu)K_1}{2E} \sqrt{\frac{r}{2\pi}} \left[(2k + 1) \sin \frac{\theta}{2} - \sin \frac{3\theta}{2} \right], \quad (14)$$

$$V = \frac{(1 + \nu)K_1}{2E} \sqrt{\frac{r}{2\pi}} \left[(2k - 1) \cos \frac{\theta}{2} - \cos \frac{3\theta}{2} \right], \quad (15)$$

$$W = \frac{-\nu h K_1}{E} \sqrt{\frac{1}{2\pi r}} \cos \frac{\theta}{2}, \quad (16)$$

where ν is Poisson's ratio, E is Young's modulus, k equals to $(3 - \nu)/(1 + \nu)$, h is the thickness of the specimen, and K_1 is the stress intensity factor corresponding to the pure mode-I fracture under three-point bending case [31]. The value of K_1 was assumed to be 1 in the simulation, because it is a constant term under a certain load, and it has no influence on the general shape, the orientation, and the symmetry properties of the simulated surface strain fields.

The pixel shearing amount can be calculated from the distance between the sheared crack-tips of the two object beams u_{11} and u_{12} . By taking this shearing value as the vertical pixel gradient step size Δy , the simulated out-of-plane and in-plane crack-tip strain components $\partial \Delta l_z / \partial y$ and $\partial \Delta l_x / \partial y$ can be obtained from the displacement fields W and U , respectively, as shown in Figs. 5(b) and 5(d). Due to the crack-tip singularity, the singular crack tip strain of the simulated $\partial \Delta l_z / \partial y$ has been eliminated for comparison, as shown in Fig. 5(b). The figure shows that the theoretical out-of-plane strain field $\partial \Delta l_x / \partial y$ is symmetric with respect to the y -axis, and

the in-plane strain field $\partial \Delta l_x / \partial y$ is antisymmetric. Hence, the general shape, the orientation, and especially the symmetry properties of the measured surface strain fields using the proposed dual-sensitive shearography agree with the theoretical results, considering the existence of stress singularity on the crack-tip area and the non-uniformity of the material.

3.3. Discussions

In the phase retrieval for dynamic measurement of crack-tip deformation fields with high strain gradient, two improvements were made in the proposed system to obtain a higher phase quality. Firstly, two slits were used as the optical spatial filters. Temporal phase shifting is limited by phase-stepping procedures, so generally it is used for quasi-static measurements. For spatial-carrier phase-shifting methods, apertures [12, 13, 25] are the most commonly used spatial filters, and this type of filter can be used to build spatial carriers in multiple directions for multi-component measurements. However, after passing through the aperture, the amount of light incident on the detector is limited, which may not enable obtaining a high phase quality. Instead, the slit filters allow more incident light so that the phase quality is improved. Secondly, a common-path shearing interferometer with a Wollaston prism as shearing device was used in this system. As compared to other shearing measurement devices such as a Michelson or a Mach-Zehnder interferometer, the developed setup is less sensitive to vibration, which increases the phase quality.

The second limitation is the synchronous acquisition of the two shearograms. To perform simultaneous and dynamic in-plane and out-of-plane strain measurements using a single-wavelength system, apart from the spatial multiplexing scheme, another possibility is to make the left and the right shearograms with different carrier frequencies overlap with each other completely on the camera without spatial separation. As a result, the phase maps relating to the left and right sensitivity vectors can be retrieved separately using the non-overlapping spectra with different carrier frequencies on condition that the interference between the left and the right object beams can be avoided effectively. However, it may not be possible to eliminate the influence of this interference completely. Thereby, at present spatial multiplexing is a reasonable choice for simultaneous and dynamic multi-component measurements.

4. Conclusion

A real-time dual-sensitive shearography system with a single-wavelength laser was developed for simultaneous and dynamic in-plane and out-of-plane strain measurements. The shearography system is capable of measuring crack-tip deformation fields. Firstly, with the introduction of the spatial multiplexing based on Fourier transform, the developed shearography system is no longer limited by phase-stepping procedures. Secondly, by the adoption of two slit spatial filters and the common-path shearing interferometer, the developed shearography system is capable of measuring deformation with high strain gradient. In experimental studies, a mode-I fracture deformation under three-point bending was measured in real time and the results agreed with the analytical solution, which shows the feasibility of the developed shearography system. Furthermore, this technique provides potential industrial applications such as real-time dynamic in-plane and out-of-plane dual-sensitive nondestructive testing.

Funding

China Scholarship Council (CSC) (201706030161, 201507090066, 201408080029, 201706050026), National Natural Science Foundation of China (Grant Nos. 11572041, 11372037, and 11232008).

References

1. H. M. Shang, Y. Hung, W. Luo, and F. Chen, "Surface profiling using shearography," *Opt. Eng.* **39**, 23–32 (2000).

2. I. Yamaguchi, J.-i. Kato, and S. Ohta, "Surface shape measurement by phase-shifting digital holography," *Opt. Rev.* **8**, 85–89 (2001).
3. U. P. Kumar, B. Bhaduri, M. P. Kothiyal, and N. K. Mohan, "Two-wavelength micro-interferometry for 3-D surface profiling," *Opt. Lasers Eng.* **47**, 223–229 (2009).
4. L. Bilgeri, F. S. Bloise, M. Lu, S. Wang, M. Jakobi, and A. W. Koch, "Intensity distortions due to phase-only spatial light modulation: Characterization for applications in electronic speckle-pattern interferometry," *Rev. Sci. Instruments* **89**, 083701 (2018).
5. N. Werth, F. S. Bloise, and A. W. Koch, "Influence of roughness in the phase-shifting speckle method: An experimental study with applications," *Rev. Sci. Instruments* **85**, 015114 (2014).
6. J. Leendertz, "Interferometric displacement measurement on scattering surfaces utilizing speckle effect," *J. Phys. E: Sci. Instruments* **3**, 214–218 (1970).
7. J. Butters and J. Leendertz, "Speckle pattern and holographic techniques in engineering metrology," *Opt. Lasers Eng.* **3**, 26–30 (1971).
8. A. W. Koch, M. W. Ruprecht, O. Toedter, and G. Häusler, *Optische messtechnik an technischen oberflächen* (Expert-Verlag: Renningen-Malmsheim, Germany, 1998).
9. J. Leendertz and J. Butters, "An image-shearing speckle-pattern interferometer for measuring bending moments," *J. Phys. E: Sci. Instruments* **6**, 1107–1110 (1973).
10. Y. Hung and C. Liang, "Image-shearing camera for direct measurement of surface strains," *Appl. Opt.* **18**, 1046–1051 (1979).
11. B. Bhaduri, M. Kothiyal, and N. K. Mohan, "Curvature measurement using three-aperture digital shearography and fast fourier transform," *Opt. Lasers Eng.* **45**, 1001–1004 (2007).
12. M. Lu, S. Wang, L. Aulbach, and A. W. Koch, "Simultaneous displacement and slope measurement in electronic speckle pattern interferometry using adjustable aperture multiplexing," *Appl. Opt.* **55**, 5868–5875 (2016).
13. M. Lu, S. Wang, L. Bilgeri, X. Song, M. Jakobi, and A. W. Koch, "Online 3D displacement measurement using speckle interferometer with a single illumination-detection path," *Sensors (Basel, Switzerland)* **18**, 1923 (2018).
14. L. Yang, W. Steinchen, M. Schuth, and G. Kupfer, "Precision measurement and nondestructive testing by means of digital phase shifting speckle pattern and speckle pattern shearing interferometry," *Measurement* **16**, 149–160 (1995).
15. B. Bhaduri, N. K. Mohan, and M. Kothiyal, "A dual-function espi system for the measurement of out-of-plane displacement and slope," *Opt. Lasers Eng.* **44**, 637–644 (2006).
16. H. V. Tippur, "Simultaneous and real-time measurement of slope and curvature fringes in thin structures using shearing interferometry," *Opt. Eng.* **43**, 3014–3021 (2004).
17. D. Sharma, R. Sirohi, and M. P. Kothiyal, "Simultaneous measurement of slope and curvature with a three-aperture speckle shearing interferometer," *Appl. Opt.* **23**, 1542–1546 (1984).
18. K. Patorski and A. G. Olszak, "Digital in-plane electronic speckle pattern shearing interferometry," *Opt. Eng.* **36**, 2010–2016 (1997).
19. G. Pedrini, Y.-L. Zou, and H. Tiziani, "Simultaneous quantitative evaluation of in-plane and out-of-plane deformations by use of a multidirectional spatial carrier," *Appl. Opt.* **36**, 786–792 (1997).
20. P. Picart, E. Moisson, and D. Mounier, "Twin-sensitivity measurement by spatial multiplexing of digitally recorded holograms," *Appl. Opt.* **42**, 1947–1957 (2003).
21. M. Mello, S. Hong, and A. Rosakis, "Extension of the coherent gradient sensor (cgs) to the combined measurement of in-plane and out-of-plane displacement field gradients," *Exp. Mech.* **49**, 277–289 (2009).
22. M. Mello and A. J. Rosakis, "Surface characterization based on lateral shearing of diffracted wave fronts to measure in-plane and out-of-plane displacement gradient fields," (2009). US Patent 7538891B1.
23. D. Francis, S. James, and R. Tatam, "Surface strain measurement using multi-component shearography with coherent fibre-optic imaging bundles," *Meas. Sci. Technol.* **18**, 3583–3591 (2007).
24. S. Wang, M. Lu, L. M. Bilgeri, M. Jakobi, F. S. Bloise, and A. W. Koch, "Temporal electronic speckle pattern interferometry for real-time in-plane rotation analysis," *Opt. Express* **26**, 8744–8755 (2018).
25. M. Lu, S. Wang, L. Aulbach, M. Jakobi, and A. W. Koch, "Non-phase unwrapping interferometric approach for a real-time in-plane rotation measurement," *Opt. Lett.* **42**, 1986–1989 (2017).
26. Y. Hung and J. Wang, "Dual-beam phase shift shearography for measurement of in-plane strains," *Opt. Lasers Eng.* **24**, 403–413 (1996).
27. X. Xie, X. Chen, J. Li, Y. Wang, and L. Yang, "Measurement of in-plane strain with dual beam spatial phase-shift digital shearography," *Meas. Sci. Technol.* **26**, 115202 (2015).
28. X. Gao, L. Yang, Y. Wang, B. Zhang, X. Dan, J. Li, and S. Wu, "Spatial phase-shift dual-beam speckle interferometry," *Appl. Opt.* **57**, 414–419 (2018).
29. W. Steinchen, L. Yang, and M. Schuth, "TV-shearography for measuring 3D-strains," *Strain* **32**, 49–58 (1996).
30. M. Takeda, H. Ina, and S. Kobayashi, "Fourier-transform method of fringe-pattern analysis for computer-based topography and interferometry," *JOSA A* **72**, 156–160 (1982).
31. H. Tada, P. C. Paris, and G. R. Irwin, "The stress analysis of cracks," *Handbook*, (Del Research Corporation, 1973).